

STAR FORMATION RATE AND DYNAMICAL MASS OF 10^8 SOLAR MASS BLACK HOLE HOST GALAXIES AT REDSHIFT 6

CHRIS J. WILLOTT

NRC Herzberg, 5071 West Saanich Rd, Victoria, BC V9E 2E7, Canada

JACQUELINE BERGERON AND ALAIN OMONT

UPMC Univ Paris 06 and CNRS, UMR7095, Institut d'Astrophysique de Paris, F-75014, Paris, France

Draft version January 30, 2015

ABSTRACT

We present ALMA observations of two moderate luminosity quasars at redshift 6. These quasars from the Canada-France High-z Quasar Survey (CFHQS) have black hole masses of $\sim 10^8 M_{\odot}$. Both quasars are detected in the [C II] line and dust continuum. Combining these data with our previous study of two similar CFHQS quasars we investigate the population properties. We show that $z > 6$ quasars have a significantly lower far-infrared luminosity than bolometric-luminosity-matched samples at lower redshift, inferring a lower star formation rate, possibly correlated with the lower black hole masses at $z = 6$. The ratios of [C II] to far-infrared luminosities in the CFHQS quasars are comparable with those of starbursts of similar star formation rate in the local universe. We determine values of velocity dispersion and dynamical mass for the quasar host galaxies based on the [C II] data. We find that there is no significant offset from the relations defined by nearby galaxies with similar black hole masses. There is however a marked increase in the scatter at $z = 6$, beyond the large observational uncertainties.

Subject headings: cosmology: observations — galaxies: evolution — galaxies: high-redshift — quasars: general

1. INTRODUCTION

Improved astronomical observational facilities have enabled the discovery and study of many galaxies at an early phase of the Universe's history. It is now possible to witness the majority of the stellar and black hole mass growth over cosmic time and identify how physical conditions at early times differ from now. One of the major relations to be determined as a function of time is the tight correlation between black hole mass and galaxy properties observed for nearby galaxies (see Kormendy & Ho 2013 for a review). Observations of this relation at high-redshift are critical to understanding the cause because most of the growth occurred at early times.

Attempts to measure black hole and galaxy masses at high-redshift face a number of problems. Black hole mass measurements cannot be made directly by resolved kinematics of gas or stars within the black hole's sphere of influence, nor by reverberation mapping. Instead black hole masses, M_{BH} , of quasars can be measured at any redshift using the single-epoch virial mass estimator that involves measuring a low-ionization broad emission line, such as Mg II or H β , and calibrating the location of the emitting gas with low- z reverberation-mapped quasars (Wandel et al. 1999). For AGN with obscured broad lines M_{BH} can only be estimated from the luminosity making an assumption about the accretion rate relative to the Eddington limit.

Measuring galaxy properties, such as luminosity or velocity dispersion, σ , of distant quasars is hampered by surface brightness dimming, the bright glare of the quasar and AGN (active galactic nuclei) emission line-contamination of spectral features. Up to $z \approx 1$ there

has been considerable success in measuring AGN host galaxy luminosities, morphologies and in some cases velocity dispersions (Cisternas et al. 2011; Park et al. 2014). At higher redshifts ($1 < z < 4$) the galaxy light is more difficult to separate from the quasar, which, combined with greater mass-to-light corrections, lead to larger uncertainties (Merloni et al. 2010; Targent et al. 2012). The results of these studies are mixed with some evidence in favour of higher M_{BH} at a given galaxy mass.

At yet higher redshifts it has proved impossible to measure the galaxy light of quasars (Mechtley et al. 2012) before launch of the *James Webb Space Telescope* and instead the main method of determining galaxy mass is kinematics of cool gas in star-forming regions (Carilli & Walter 2013). Facilities such as the IRAM Plateau de Bure Interferometer, the Jansky Very Large Array and the Atacama Large Millimeter Array (ALMA) have sufficient sensitivity and resolution to resolve the gas in distant quasar hosts and provide dynamical masses (Walter et al. 2004, 2009; Wang et al. 2010, 2013). In particular, ALMA has the sensitivity to probe $z = 6$ quasar hosts with star formation rates, SFR, in the tens of solar masses per year, rather than only in the extreme starbursts previously observable (Willott et al. 2013). The studies above focussed on $z \approx 6$ Sloan Digital Sky Survey (SDSS) and UKIRT Infrared Deep Sky Survey (UKIDSS) quasars with high UV and far-IR luminosities and found that their black holes are on average 10 times greater than the corresponding σ for local galaxies, roughly consistent with a continuation of the evolution seen in lower redshift studies.

Although observationally there appears to be an increase in M_{BH} with redshift at a given galaxy mass or σ , it has long been understood that there are selection

biases that affect how closely the observations trace the underlying distribution. In particular, the steepness of the galaxy and dark matter mass functions combined with large scatter in their correlations with black hole mass mean that a high black-hole-mass-selected sample of quasars will have a systematic offset in σ towards lower values. This effect, first identified by Willott et al. (2005) and Fine et al. (2006) was studied in detail in Lauer et al. (2007) and numerous studies thereafter. The magnitude of the effect depends upon the scatter in the correlation, which has not been conclusively measured at high-redshift, but appears to increase with redshift (Schulze & Wisotzki 2014). Willott et al. (2005) and Lauer et al. (2007) showed that the bias is particularly strong for $M_{\text{BH}} > 10^9 M_{\odot}$ quasars such as those in the SDSS at $z \approx 6$ and therefore that the factor of 10 increase in M_{BH} at a given σ first seen in the quasar SDSS J1148+5251 (Walter et al. 2004) could be accounted for by the bias (see also Schulze & Wisotzki 2014). In comparison, there would be little bias for a sample of high- z quasars with black hole masses of $M_{\text{BH}} \sim 10^8 M_{\odot}$ (Lauer et al. 2007).

An alternative to measuring the evolution of the assembled galaxy and black hole masses is to determine the rate at which mass growth is occurring. For quasars the bolometric luminosity is a measure of the black hole mass growth rate. For galaxies, the star formation rate is proportional to the stellar mass growth. The star formation rate can be determined by the rest-frame far-infrared dust continuum luminosity. Additionally, the interstellar [C II] far-infrared emission line is well-correlated with star-formation (De Looze et al. 2014; Sargsyan et al. 2014) so can also be used as a star formation proxy.

In Willott et al. (2013, hereafter Wi13) we presented Cycle 0 ALMA observations in the [C II] line and 1.2 mm continuum for two $z = 6.4$ quasars from the Canada-France-High- z Quasar Survey (CFHQS, Willott et al. 2010b). These quasars have $M_{\text{BH}} \sim 10^8 M_{\odot}$, a factor of 10–30 lower than most SDSS quasars known at these redshifts. One quasar was detected in line and continuum and the other remained undetected in these sensitive observations placing an upper limit on its star formation rate of $\text{SFR} < 40 M_{\odot} \text{ yr}^{-1}$.

In this paper we present ALMA observations of two further CFHQS quasars with similar redshift and black hole mass with the aim of providing a sample large enough to address the issue of how host galaxy properties such as SFR, σ and dynamical mass depend upon black hole accretion rate and mass at a time just 1 billion years after the Big Bang. In particular, these quasars are not subject to the bias in the $M_{\text{BH}} - \sigma$ relation discussed previously because of their moderate black hole masses. Cosmological parameters of $H_0 = 67.8 \text{ km s}^{-1} \text{ Mpc}^{-1}$, $\Omega_{\text{M}} = 0.307$ and $\Omega_{\Lambda} = 0.693$ (Planck Collaboration 2014) are assumed throughout.

2. OBSERVATIONS

CFHQS J005502+014618 (hereafter J0055+0146) and CFHQS J222901+145709 (hereafter J2229+1457) were observed with ALMA on the 28, 29 and 30 November 2013 for Cycle 1 project 2012.1.00676.S. Between 22 and 26 12 m diameter antennae were used. The typical long baselines were ~ 400 m providing similar spatial resolution to our Cycle 0 observations. Observations of the science targets were interleaved with nearby phase calibra-

tors, J0108+0135 and J2232+1143. The amplitude calibrator was Neptune and the bandpass calibrators J2258-2758 and J2148+0657. Total on-source integration times were 4610 s for J0055+0146 and 5490 s for J2229+1457.

The band 6 (1.3 mm) receivers were set to cover the frequency range of the redshifted [C II] transition ($\nu_{\text{rest}} = 1900.5369 \text{ GHz}$) and sample the dust continuum. There are four $\approx 2 \text{ GHz}$ basebands, two pairs of adjacent bands with a 11 GHz gap in between. The channel width is 15.625 MHz (17 km s^{-1}).

The data were initially processed by North American ALMA Regional Center staff with the CASA software package¹. On inspection of these data it became clear that the [C II] line of J0055+0146 was located right at the edge of the baseband, 1000 km s^{-1} from the targeted frequency defined by the broad, low-ionization Mg II emission line ($z_{\text{MgII}} = 5.983$; Willott et al. 2010a). The Mg II line redshift is usually close to the systemic redshift as measured by narrow optical lines with a dispersion of 270 km s^{-1} (Richards et al. 2002). A large offset for this quasar was not particularly surprising for two reasons: firstly the signal-to-noise (SNR) of the Mg II detection is not very high and the line appears double-peaked due to noise and/or associated absorption; secondly the Ly α redshift ($z_{\text{Ly}\alpha} = 6.02$) is offset from Mg II by 1600 km s^{-1} (in the same direction as the [C II] offset) and this would make the size of the Ly α ionized near-zone negative, which is not physically sensible for a quasar with such a high ionizing flux and has not been observed in a sample of $27 z \approx 6$ quasars (Carilli et al. 2010). Due to this redshift uncertainty the receiver basebands were set up so that the adjacent band covered the Ly α redshift with zero gap between the two bands.

The default ALMA Regional Center reduction excluded 11 channels at each end of the 128 channel band. However, only the first 4 channels need to be excluded, so we re-reduced the data with CASA to include more spectral channels at the baseband edges. We checked that the noise does not increase in these extra channels, except for the very first and last channels to contain data so we excluded those. In summary our reduced product contains 118 of the original 128 channels per baseband, compared with 106 channels in the default reduction.

3. RESULTS

Figure 1 shows the reduced spectrum of J0055+0146 from the two adjacent basebands. The final gap between the bands is only $\approx 150 \text{ km s}^{-1}$ and crucially the peak of the [C II] line is contained within the higher frequency band. The lower frequency band contains only a small amount of the line flux but provides an important constraint on the wings and hence the peak and width for a symmetric line. A single Gaussian plus flat continuum model was fit to the available data using a Markov-Chain Monte Carlo (MCMC). This process shows a good fit for a single Gaussian with $\text{FWHM} = 359 \pm 27 \text{ km s}^{-1}$. The formal uncertainty in the FWHM is very small considering that there is some missing data. This is because a symmetric line model is used and with the peak and wings covered by data there is little margin for deviation in the missing channels. We add in quadrature an extra 10% uncertainty in both the line flux and FWHM due to

¹ <http://casa.nrao.edu>

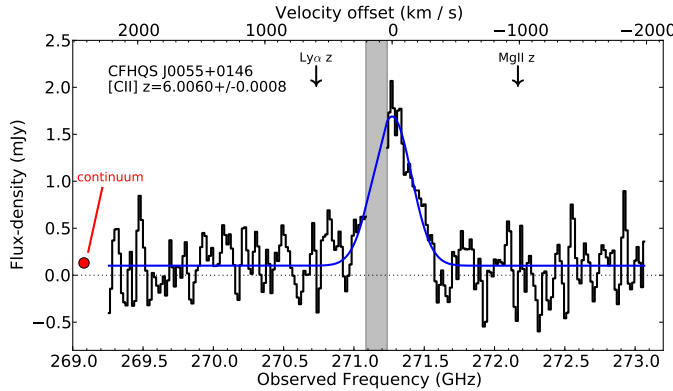


FIG. 1.— ALMA spectrum of J0055+0146 covering two adjacent basebands. The gap between the bands with no data is shaded in gray. The higher frequency band is centred on the redshift determined from the Mg II emission line whereas the lower frequency band covers the Ly α redshift. The [C II] line is found at the edge of the higher frequency band. The blue curve is a Gaussian plus continuum fit as described in the text. The red circle marks the continuum level independently measured in the three line-free basebands. The upper axis is the velocity offset from the best-fit [C II] Gaussian peak.

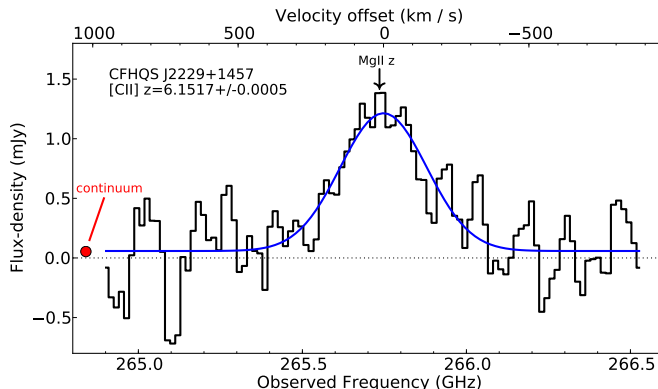


FIG. 2.— ALMA spectrum of J2229+1457 covering the single baseband containing the [C II] line. The blue curve is a Gaussian plus continuum fit and the red circle the independent continuum level. The upper axis is the velocity offset from the best-fit [C II] Gaussian peak.

the missing channels.

The spectrum of J2229+1457 is plotted in Figure 2. For this quasar the [C II] line is centred in the band with no significant offset from the Mg II redshift. The line is consistent with a single Gaussian with a best fit $\text{FWHM} = 351 \pm 39 \text{ km s}^{-1}$, similar to the value for J0055+0146. The continuum level of the fit is again consistent with the independent continuum level determined from the three line-free basebands. Measurements from the spectra are given in Table 1.

Figure 3 shows maps of the 1.2 mm continuum (white contours) plus the [C II] line (color scale) for the quasars. For both quasars there is no significant offset between any of the continuum or line centroids or the optical quasar position. The $< 1''$ mm-optical offset is within the relative uncertainty of the optical astrometry. The more accurate [C II] positions for the two quasars are $00:55:02.92 +01.46.17.80$ and $22:29:01.66 +14.57.08.30$. For J2229+1457 there is only a marginal 2σ detection of the continuum located coincident with the peak of the line emission. As seen in Figure 3 there are several other continuum peaks of this magnitude or greater in

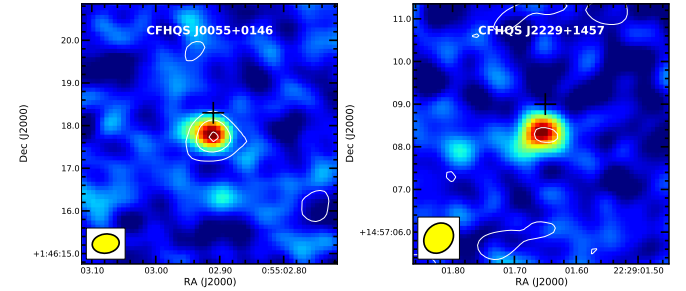


FIG. 3.— The color scale shows the integrated [C II] line maps for the two quasars. White contours of 1.2 mm continuum emission from the three line-free basebands are over-plotted at levels of $2, 4, 6 \sigma \text{ beam}^{-1}$. The quasar optical positions are shown with a black plus symbol. The positional offsets between the optical and millimeter are most likely due to astrometric mismatch, rather than a physical offset. J0055+0146 is well-detected in both continuum and line emission. J2229+1457 has only a 2σ continuum detection that is spatially co-incident with the line emission. The restoring beam is shown in yellow in the lower-left corner.

TABLE 1
MILLIMETER DATA FOR THE TWO CFHQS QUASARS

	CFHQS J0055+0146	CFHQS J2229+1457
$z_{\text{MgII}}^{\text{a}}$	5.983 ± 0.004	6.152 ± 0.003
$z_{[\text{CII}]}$	6.0060 ± 0.0008	6.1517 ± 0.0005
$\text{FWHM}_{[\text{CII}]}$	$359 \pm 45 \text{ km s}^{-1}$	$351 \pm 39 \text{ km s}^{-1}$
$I_{[\text{CII}]} (\text{Jy km s}^{-1})$	0.839 ± 0.132	0.582 ± 0.075
$L_{[\text{CII}]} (L_{\odot})$	$(8.27 \pm 1.30) \times 10^8$	$(5.96 \pm 0.77) \times 10^8$
$f_{1.2\text{mm}} (\mu\text{Jy})$	211 ± 34	54 ± 29
$L_{\text{FIR}} (L_{\odot})$	$(4.85 \pm 0.78) \times 10^{11}$	$(1.24 \pm 0.67) \times 10^{11}$
$\text{SFR}_{[\text{CII}]} (M_{\odot} \text{ yr}^{-1})$	83 ± 13	60 ± 8
$\text{SFR}_{\text{FIR}} (M_{\odot} \text{ yr}^{-1})$	73 ± 12	19 ± 10
$L_{[\text{CII}]} / L_{\text{FIR}}$	$(1.70 \pm 0.38) \times 10^{-3}$	$(4.80 \pm 2.67) \times 10^{-3}$

NOTES.—

^a Derived from Mg II $\lambda 2799$ observations (Willott et al. 2010a). Uncertainties in L_{FIR} , $\text{SFR}_{[\text{CII}]}$ and SFR_{FIR} only include measurement uncertainties, not the uncertainties in extrapolating from a monochromatic to integrated luminosity or that of the luminosity-SFR calibrations.

the vicinity, so it is not considered a secure detection, however the measured flux and uncertainty are included in Table 1.

The quasar 1.2 mm continuum flux-densities were converted to far-infrared luminosity, L_{FIR} , assuming a typical SED for high-redshift star-forming galaxies. As in Wi13 we adopt a greybody spectrum with dust temperature, $T_d = 47 \text{ K}$ and emissivity index, $\beta = 1.6$. To convert from far-IR luminosity to star formation rate we use the relation $\text{SFR} (M_{\odot} \text{ yr}^{-1}) = 1.5 \times 10^{-10} L_{\text{FIR}} (L_{\odot})$ appropriate for a Chabrier IMF (Carilli & Walter 2013). We note that this assumes that all the dust contributing to the 1.2 mm continuum is heated by hot stars and not by the quasar. An alternative estimate of the star formation rate comes from the [C II] luminosity. We adopt the relation in Sargsyan et al. (2014) of $\text{SFR} (M_{\odot} \text{ yr}^{-1}) = 1.0 \times 10^{-7} L_{[\text{CII}]} (L_{\odot})$. For the remainder of this paper, uncertainties on L_{FIR} (and inferred SFR) only include the flux measurement uncertainties, not that of the dust temperature and luminosity to SFR conversion.

The synthesized beam sizes are $0''.63$ by $0''.45$ for J0055+0146 and $0''.76$ by $0''.64$ for J2229+1457. The better resolution for J0055+0146 is mostly due to higher elevation of observation. We used the CASA IMFIT task to fit 2D gaussian models to these maps. For J0055 both

the continuum and line are resolved with deconvolved source sizes of $0''.51 \pm 0''.13$ by $0''.35 \pm 0''.26$ at position angle 87 degrees and $0''.50 \pm 0''.14$ by $0''.18 \pm 0''.27$ at position angle 62 degrees, respectively. At the distance to this quasar the spatial extent of $0.5''$ is equal to a linear size of 2.9 kpc. We note that the missing data in the red wing of the [C II] line may cause a bias in the size and inclination if the emission comes from a rotating disk, but there is no evidence for this based on the similarity of the line and continuum sizes. For J2229+1457 the continuum is too poorly detected to attempt a size measurement and the line emission is only marginally more extended than the beam size. In several other $z \approx 6$ quasars velocity gradients across the sources are observed (Wi13; Wang et al. 2013). Velocity gradients are not seen for either of these two quasars, although for J0055+0146 the missing data for 150 km s^{-1} of the red wing hampers our ability to detect such a gradient.

4. DISCUSSION

4.1. Evolution of far-IR luminosity

In Wi13 we reported on the low far-IR luminosities of the two previously observed CFHQS quasars and implications for the relatively low SFR of these quasar host galaxies relative to the black hole accretion rate. We now revisit this issue with the sample of four $z \approx 6$ CFHQS quasars with ALMA observations. We note that this sample includes four of the six CFHQS quasars with measured black hole masses within the absolute magnitude range $-25.5 < M_{1450} < -24$ at a declination low enough for ALMA observation. The two unobserved quasars have $7 \times 10^8 < M_{\text{BH}} < 10^9 M_{\odot}$, and were not observed due to limited time available and the desire to study the lowest mass black holes from CFHQS. Therefore there is a slight bias to low black hole mass in this sample compared to pure UV-luminosity-selection.

Two of the four quasars are well detected in the continuum with fluxes of 211 ± 34 (J0055+0146) and 120 ± 35 (J0210-0456) μJy . J2229 has a marginal 2σ detection of $54 \pm 29 \mu\text{Jy}$ (Figure 3 and Table 1) and J2329-0301 is undetected with a 1σ rms of $30 \mu\text{Jy}$. We combine the four values of far-infrared luminosity derived from these measurements assuming that J2329-0301 has a flux equal to its 2σ upper limit of $60 \mu\text{Jy}$. The mean and standard deviation of the sample is $L_{\text{FIR}} = (2.6 \pm 1.4) \times 10^{11} L_{\odot}$. We note this is much lower than the values of $10^{12} - 10^{13} L_{\odot}$ typically discussed for $z \approx 6$ quasars due to two factors, firstly that the CFHQS sample here have lower AGN luminosity than most known $z \approx 6$ quasars and a correlation between AGN and far-IR luminosities is present (Wang et al. 2011; Omont et al. 2013), but also that our small sample is selected on quasar rest-frame UV luminosity and black hole mass, whereas previous studies have focussed on quasars with pre-ALMA millimeter continuum detections.

The implication is that these quasars have very high black hole accretion rates as inferred from the AGN bolometric luminosity, L_{Bol} , yet relatively low SFR. Such a scenario is consistent with the well-known evolutionary model whereby the optical quasar phase comes after the main star forming phase (Khandai et al. 2012; Lapi et al. 2014), possibly due to quasar feedback inhibiting gas cooling and star formation. The measured ratio of $L_{\text{FIR}}/L_{\text{Bol}} = 0.035$ for the four CFHQS quasars is only

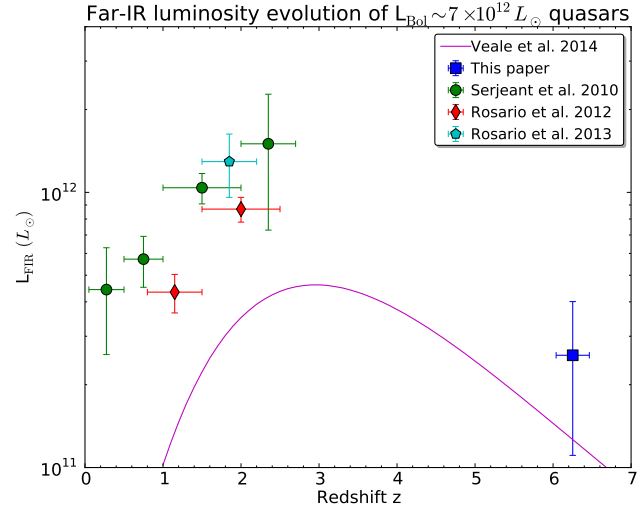


FIG. 4.— Stacked mean far-infrared luminosity for samples of quasars at different redshifts. Details of the samples are described in the text, but all samples are selected to include roughly the same range in bolometric luminosity centred on $L_{\text{Bol}} \sim 7 \times 10^{12} L_{\odot}$, the mean L_{Bol} of the four $z \approx 6$ CFHQS quasars plotted with the blue square. There is a clear rise in L_{FIR} up to a peak at $2 < z < 3$ followed by a decline to $z = 6$. The magenta curve shows the mean L_{FIR} due to star formation for the model of Veale et al. (2014) including scaling by a factor of 2 to account for stellar mass loss.

found in the optical quasar phase of co-evolution at a time ~ 1 Gyr after the onset of activity for the $z = 2$ model of Lapi et al. (2014). Given that this is the age of the universe at $z = 6$ the evolution must occur more rapidly at higher redshift. However, the effect of AGN variability may also be important leading to a selection effect whereby AGN luminosity-selected objects are observed to have lower ratios of $L_{\text{FIR}}/L_{\text{Bol}}$ than the time-averaged values (Hickox et al. 2014; Veale et al. 2014).

We have previously shown (Wi13) that the two $z = 6.4$ CFHQS quasars observed with ALMA in Cycle 0 have L_{FIR} lower than quasars of similar AGN luminosity at lower redshift. On the other hand, at fixed AGN luminosity L_{FIR} is observed to rise from $z = 0$ to $z = 3$ (Serjeant et al. 2010; Bonfield et al. 2011; Rosario et al. 2012, 2013). We next analyze the evolution of L_{FIR} using our expanded ALMA sample at $z = 6$ and comparable low-redshift data. At all redshifts we determine the mean L_{FIR} for optically-selected quasars and X-ray AGN in a narrow range of L_{Bol} corresponding to the mean L_{Bol} of the four CFHQS $z \approx 6$ quasars in this paper ($L_{\text{Bol}} \sim 7 \times 10^{12} L_{\odot}$).

At $z < 3$ we use three datasets based on *Herschel* imaging of AGN. Serjeant et al. (2010) stacked *Herschel* SPIRE data of optically-selected quasars and quoted their results as rest-frame $100 \mu\text{m}$ luminosity. We adopt $L_{\text{FIR}} = 1.43 \nu L_{\nu}(100 \mu\text{m})$ (Chary & Elbaz 2001) to convert to far-infrared luminosity. The absolute magnitude bin $-26 < I_{\text{AB}} < -24$ corresponds well to $L_{\text{Bol}} \sim 7 \times 10^{12} L_{\odot}$ and we have trimmed the size of the highest redshift bin from $2 < z < 4$ to $2 < z < 2.7$ because inspection of the luminosity-redshift plane figure in Serjeant et al. (2010) shows all but one of the 52 quasars in this bin are at $z < 2.7$. Rosario et al. (2013) analyzed the *Herschel* PACS data for optically-selected quasars in COSMOS. Due to the shorter wavelength of

PACS than SPIRE they presented results in rest-frame $60\mu\text{m}$ luminosity. We adopt $L_{\text{FIR}} = 1.5\nu L_{\nu}(60\mu\text{m})$ (Chary & Elbaz 2001) to convert to far-infrared luminosity. From this study we use only the highest redshift, highest luminosity bin as this compares well with $L_{\text{Bol}} \sim 7 \times 10^{12} L_{\odot}$. Rosario et al. (2012) determined the mean infrared luminosity with PACS for X-ray-selected AGN from the COSMOS survey. We note that the X-ray selected AGN sample contains a mixture of broad-line, narrow-line and lineless AGN and these may have different evolutionary properties, but Rosario et al. (2013) showed that the mean L_{FIR} of quasars and X-ray-selected are similar at a given AGN luminosity and redshift. We use the Rosario et al. (2012) data from the AGN luminosity bin $8 \times 10^{11} < L_{\text{Bol}} < 2 \times 10^{13} L_{\odot}$. Whilst most sources in this bin have $L_{\text{Bol}} < 3 \times 10^{12} L_{\odot}$, we consider the results appropriate to compare to the $z \approx 6$ quasars as the correlation between L_{FIR} and L_{Bol} is very shallow at this luminosity in Rosario et al. (2012).

Figure 4 plots data from these three low-redshift studies with the CFHQS ALMA bin at $6 < z < 6.5$. The three low-redshift studies show a rise in L_{FIR} of a factor of 4 from $z = 0.3$ to $z = 2.4$. This rise is attributed to the general increase in massive galaxy specific star formation rate over this redshift range (Hickox et al. 2014). The $6 < z < 6.5$ bin has a large dispersion due to the range in 1.2 mm continuum flux measured for the 4 quasars. The mean L_{FIR} at $z \approx 6$ is a factor of about 2 lower than the $z = 0.3$ bin and 6 lower than the $z = 2.4$ peak at the so-called *quasar epoch*. There is clear evidence here for a turnaround that mimics the evolution of the quasar luminosity function (McGreer et al. 2013) and star formation rate density (Bouwens et al. 2014), albeit with a much less steep high-redshift decline due to the fact we are measuring star formation in special locations within the universe where dark matter halos must have collapsed much earlier than typical in order to build up the observed black hole masses of $\sim 10^8 M_{\odot}$.

What is the physical reason for this turnaround at $z > 3$? In the evolutionary picture where the optical quasar phase follows the starburst phase one would expect the star formation and black hole accretion to be more tightly coupled at high-redshift where there is barely enough time for star formation to have decreased substantially. A clue may come from one of the few differences between quasars at these two epochs. Willott et al. (2010a) showed that the Eddington ratios of matched quasar luminosity samples at $z = 2$ and $z = 6$ are significantly different with the $z = 6$ quasars having a factor of $3 \times$ higher Eddington ratios and therefore $3 \times$ lower black hole masses than at $z = 2$. Such a difference exists between the typical black hole mass of our CFHQS ALMA sample and that of the highest luminosity bin of Rosario et al. (2013). This Eddington ratio evolution is observed in other studies (De Rosa et al. 2011; Trakhtenbrot et al. 2011; Shen & Kelly 2012) and predicted by many theoretical works due to the increase in gas supply to black holes at high-redshift (Sijacki et al. 2014).

In Figure 4 we also plot a theoretical curve of mean L_{FIR} versus redshift for a simulated sample of rest-frame UV-selected quasars in the same L_{Bol} range as the observed quasar samples for the model of Veale et al. (2014). This model assumes an evolving linear relationship between star formation and black hole growth. The

variant of the model plotted here is the “accretion” model where the quasar luminosity is proportional to the black hole growth rate and the Eddington ratio distribution is a truncated power-law with slope $\beta = 0.6$ (dashed curve in Figure 8 of Veale et al. 2014). The model is constrained by the observed evolving quasar luminosity function and the local ratio of black hole to galaxy mass. We have scaled this model with a factor of $2 \times$ increase in L_{FIR} to account for stellar mass loss.

As seen in Figure 4 this curve increases from low redshift to the peak quasar epoch at $2 < z < 3$ by about the same factor as the data, although the total normalization of the curve is lower by a factor of 3 to 4. Veale et al. (2014) discuss some of the reasons why the normalization may be lower than the observations. The decrease in L_{FIR} with increasing cosmic time from $z = 2$ to $z = 0$ for fixed luminosity quasars is due to the fact that such quasars are rarer at lower redshift and on the steep end of the luminosity function where scatter is more important. This behaviour also follows from the general decrease in specific star formation rate with cosmic time. The high-redshift behaviour of a decline from $z = 3$ to $z = 6$ matches our observations, so it is instructive to understand why this occurs in the model. It is due to the assumed $(1+z)^2$ evolution of the ratio of accretion growth to stellar mass growth, but this assumed evolution is also degenerate with evolution in the Eddington ratio. As discussed previously there is observational evidence for positive evolution in the Eddington ratio from $z = 2$ to $z = 6$, meaning that the ratio of accretion growth to stellar mass growth may change more gradually than $(1+z)^2$.

A possible alternative explanation for the low L_{FIR} at $z = 6$ is that at these early epochs insufficient dust has been generated so that star formation occurs more often within lower dust environments (Ouchi et al. 2013; Tan et al. 2013; Fisher et al. 2014; Ota et al. 2014). In this case there could be a much smaller decline in the typical SFR of a luminous quasar hosting galaxy. However, two lines of evidence point towards this not being the main factor for our quasar sample. First, quasars at $z = 6$ are known to have emission line ratios similar to lower redshift quasars inferring high metallicity at least close to the accreting black hole (Freudling et al. 2003). Second, the [C II] luminosities in three of the four quasars are high (see below), suggesting high carbon abundances throughout the host galaxies.

4.2. The [CII] – far-IR luminosity relation

Three of the four CFHQS ALMA quasars are detected in both [C II] line and 1.2 mm continuum emission (two new detections in this paper and J0210–0456 in Wi13). With the low L_{FIR} discussed in the previous section, these quasar host galaxies probe a new regime in L_{FIR} at high-redshift. In Figure 5 we plot the ratio of [C II] to far-IR luminosity as a function of L_{FIR} . Also plotted are several samples from the literature which, due to ALMA at high-redshift and *Herschel* at low-redshift, are rapidly increasing in size and data quality. The low-redshift $z < 0.4$ sample of galaxies is from Graciá-Carpio et al. (2011 and in prep.) and contains a mix of normal galaxies, starbursts and ultra-luminous infrared galaxies (ULIRGs), some of which contain AGN. The ULIRGs show a [CII] deficit that has been widely discussed in

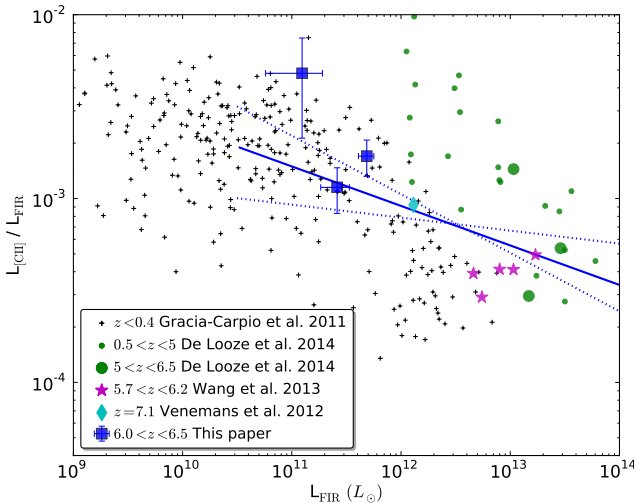


FIG. 5.— The ratio of [CII] to far-IR luminosity as a function of far-IR luminosity. High-redshift ($z > 5$) sources, mostly quasar host galaxies, are identified with large symbols. Error bars are only plotted for the CFHQs ALMA sources to enhance the clarity of the figure. The solid and dotted blue lines show the best fit power-law and 1σ uncertainty for the $z > 5$ sources. The $z > 5$ relation is largely consistent with the distribution of data at lower redshift.

the literature as due to possible factors including AGN contamination of L_{FIR} (Sargsyan et al. 2012), high gas fractions (Graciá-Carpio et al. 2011) or the dustiness, temperature and/or density of star forming regions (Farrah et al. 2013; Magdis et al. 2014). Previous observations of high L_{FIR} $z > 5$ SDSS quasars (Maiolino et al. 2005; Wang et al. 2013) showed a similar deficit. However many $0.5 < z < 5$ ULIRGs do not show this deficit and have $L_{\text{[CII]}}/L_{\text{FIR}}$ ratios comparable to low-redshift star-forming galaxies (Stacey et al. 2010). This is visible in Figure 5 for the $0.5 < z < 5$ compilation of De Looze et al. (2014).

By adding three $z > 6$ quasars with $10^{11} < L_{\text{FIR}} < 10^{12} L_{\odot}$ to Figure 5 we have greatly expanded the range of luminosities at the highest redshift. Large symbols on Figure 5 identify $z > 5$ sources. The three $z > 5$ De Looze et al. (2014) sources are HLSJ091828.6+514223 at $z = 5.24$ (Rawle et al. 2014), HFLS3 at $z = 6.34$ (Riechers et al. 2013) and SDSS J1148+5251 at $z = 6.42$ (Maiolino et al. 2005). We note that these sources were mostly selected for followup based on high L_{FIR} . The quasar ULAS J1120+0641 at $z = 7.1$ has a more moderate L_{FIR} and $L_{\text{[CII]}}/L_{\text{FIR}}$ ratio and lies in between the CFHQs and high L_{FIR} objects on the plot.

Although we are wary of the selection effects in Figure 5 and the as yet unknown cause for the change in $L_{\text{[CII]}}/L_{\text{FIR}}$ with L_{FIR} at high-redshift, the new data provide the opportunity to make the first measurement of the slope of this relation at $z > 5$. We fit the 12 $z > 5$ sources with a single power-law model of the dependence of L_{FIR} on $L_{\text{[CII]}}$ incorporating the observational (but not systematic) uncertainties using a MCMC procedure. The best-fit relation is

$$\log_{10} L_{\text{FIR}} = 0.59 + 1.27 \log_{10} L_{\text{[CII]}}. \quad (1)$$

Therefore the $L_{\text{[CII]}}/L_{\text{FIR}}$ ratio line plotted in Figure 5 has a logarithmic slope of $(1/1.27) - 1 = -0.21$. The MCMC 1σ uncertainties, based solely on the observational data, are plotted as dotted lines. These also favor a shallow negative slope, not nearly as steep as the slope that would be fit to the previous $z > 0.5$ data that covers only a narrow range of L_{FIR} . The $L_{\text{[CII]}}/L_{\text{FIR}}$ ratios of the CFHQs and ULAS $z > 6$ quasars are not greatly different to those of similar L_{FIR} galaxies at low-redshift.

Wang et al. (2013) note that the low $L_{\text{[CII]}}/L_{\text{FIR}}$ ratios for SDSS $z > 5$ quasars may be at least in part due to AGN contamination of the far-IR emission. Future observations at higher spatial resolution will be critical to examine differences in the spatial distribution of the line and continuum emission (e.g. Ciccone et al. 2014). We expect to observe that the dust continuum is more compact than the [CII] line in the high L_{FIR} $z > 5$ quasars, due to either more centrally-concentrated starbursts with higher dust temperatures, like local ULIRGs, or AGN dust-heating. In contrast we expect the low L_{FIR} $z > 5$ quasars have star formation spread more evenly throughout their host galaxies, with similar spatial distribution of line and continuum emission.

4.3. The $z \approx 6 M_{\text{BH}} - \sigma$ and $M_{\text{BH}} - M_{\text{dyn}}$ relationships

The combination of black hole mass estimates and [CII] line host galaxy dynamics for these $z \approx 6$ quasars allows us to investigate the black hole - galaxy mass correlation at an early epoch in the universe. The evolution of this relationship is a critical constraint on the co-evolution (or not) of galaxies and their nuclear black holes. As discussed in the Introduction there are reasons to believe that past studies using only the most massive black holes from SDSS quasars (e.g. Wang et al. 2010) were prone to a bias where one would expect the black holes to be relatively more massive than the galaxies (Willott et al. 2005; Lauer et al. 2007), as observed. With new data on $M_{\text{BH}} \sim 10^8 M_{\odot}$ quasars we are able to test this hypothesis and determine any real offset from the local relationship. Additionally, most previous work in this area has used the molecular CO line to trace the gas dynamics. CO is usually more centrally concentrated than [CII], so [CII] potentially probes a larger fraction of the total mass (although we note that Wang et al. 2013 found similar dynamical masses using CO and [CII] for their $z \approx 6$ quasars).

In addition to the CFHQs and Wang et al. (2013) quasars we add to our study two other $z > 6$ quasars observed in the [CII] line: SDSS J1148+5251 at $z = 6.42$ and the most distant known quasar, ULAS J1120+0641 at $z = 7.08$. Both these quasars have Mg II-derived black hole masses (De Rosa et al. 2011, 2014) with very low measurement uncertainties. The black hole masses for all three CFHQs quasars also come from Mg II measurements (Willott et al. 2010a). Some of these spectra are of moderate SNR and have substantial measurement uncertainties on the black hole masses. To all the quasars with Mg II-derived black hole masses we add a 0.3 dex uncertainty to the measurement uncertainties to account for the dispersion in the reverberation-mapped quasar calibration (Shen et al. 2008).

None of the Wang et al. (2013) quasars have Mg II measurements so black hole masses are estimated assuming that the quasars radiate at the Eddington limit, as observed for most $z \approx 6$ quasars (Jiang et al. 2007; Kurk et al. 2007; Willott et al. 2010a; De Rosa et al. 2011). The dispersion in the lognormal Eddington ratio distribution

at $z \approx 6$ is 0.3 dex (Willott et al. 2010a). We add 0.3 dex uncertainty from the observed dispersion in the Eddington ratio distribution in quadrature to the 0.3 dex due to the dispersion in the reverberation-mapped quasar calibration for a total uncertainty on the Wang et al. (2013) quasar black hole masses of 0.45 dex.

First we consider the $M_{\text{BH}} - \sigma$ relationship. For nearby galaxies σ is the velocity dispersion of the galaxy bulge. At high-redshift bulges are less common (Cassata et al. 2011) and we do not expect the $z \approx 6$ kinematics to match that of a pressure supported bulge. With the limited spatial resolution of current data we cannot be sure the [CII] gas is distributed in a rotating disk, although there is evidence of this for some sources (Wang et al. 2013). Ho (2007a) discusses the relationship and calibration of bulge velocity dispersion and disk circular velocity and concludes that although there is additional scatter one can relate molecular or atomic gas in a disk to stellar bulges. The major complication is the inclination of the disk. For a random sample of inclinations this can be modelled, however there is a possibility that quasars have disks oriented more often face-on, reducing the line-of-sight velocity dispersion (Ho 2007b).

We determine σ using the method of Ho (2007b), specifically setting the [CII] line full-width at 20% equal to $1.5 \times$ the FWHM as expected for a Gaussian since most of the lines are approximately Gaussian. The [CII] emitting gas is assumed to be in an inclined disk where the inclination angle, i , is determined by the ratio of minor (a_{min}) and major (a_{maj}) axes, $i = \cos^{-1}(a_{\text{min}}/a_{\text{maj}})$. The circular velocity is therefore $v_{\text{cir}} = 0.75 \text{ FWHM}_{\text{[CII]}} / \sin i$. For all of the quasars in this study we determine an inclination from the [CII] data or assume an inclination if one or both the major and minor axes are unresolved. All the quasars in Wang et al. (2013) were spatially resolved, although some had quite large uncertainties on a_{min} and a_{maj} . We adopt the inclination angles from their paper.

For the [CII] emission of J0210–0456, $a_{\text{maj}} = 0''.52 \pm 0''.25$ (2.9 kpc) with $i = 64^\circ$ (Wi13). For J0055+0146, $a_{\text{maj}} = 0''.50 \pm 0''.14$ (2.9 kpc) with $i = 69^\circ$ (Section 3, assuming no bias from missing red wing data). The [CII] emission of J2229+1457 is only marginally spatially resolved ($0''.85$ versus beam size of $0''.76$) and we estimate an intrinsic FWHM of $\approx 0''.4$ (2.4 kpc). An inclination of $i = 55^\circ$ is assumed as this is the median inclination angle for the resolved sources in this paper and Wang et al. (2013). Neither SDSS J1148+5251 nor ULAS J1120+0641 have published inclination angles, so we also assume $i = 55^\circ$ for both of them. We adopt $\text{FWHM}_{\text{[CII]}} = 287 \pm 28 \text{ km s}^{-1}$ for SDSS J1148+5251 (Walter et al. 2009) and $\text{FWHM}_{\text{[CII]}} = 235 \pm 35 \text{ km s}^{-1}$ for ULAS J1120+0641 (Venemans et al. 2012). Values of black hole masses and σ for this sample are provided in Table 2.

Figure 6 shows the $M_{\text{BH}} - \sigma$ relationship for the $z \approx 6$ quasar sample. Uncertainties on black hole masses include the scatter in the calibration as described previously. Uncertainties in σ include FWHM measurement uncertainty plus a 10% uncertainty for the conversion from FWHM to v_{cir} and 15% for the conversion from v_{cir} to σ as seen in the sample of Ho (2007a). The black line is the local correlation of Kormendy & Ho (2013) with the gray band the $\pm 1\sigma$ scatter. The first thing to note is that

the quasars are distributed around the local relationship rather than all being offset to low σ as is commonly believed to be the case. As noted by Wang et al. (2010), using the method of Ho (2007b), rather than calculating σ as FWHM/2.35, leads to much higher σ . Note that this is without adopting extreme face-on inclinations for most quasars. There are still several quasars, such as SDSS J1148+5251 and ULAS J1120+0641, that have values of σ considerably lower than the local relation.

The main result of Figure 6 is that whilst there is little mean shift between the $z = 0$ and $z \approx 6$ data, there is a much larger scatter in the data at $z \approx 6$, well beyond the size of the error bars. This larger scatter at an early epoch is expected based on dynamical evolution, incoherence in AGN/starburst activity and the tightening of the relation over time from merging (Peng 2007). We note that our hypothesis that the bias described in the Introduction would lead to the lower M_{BH} quasars being located on the local relation with a lower scatter than the high M_{BH} quasars is not supported by these observations. The scatter in $\log_{10} \sigma$ at $M_{\text{BH}} \approx 10^8 M_{\odot}$ is about the same as that at $M_{\text{BH}} > 10^9 M_{\odot}$.

We go one step further from σ to determine dynamical masses using the deconvolved [CII] sizes. For consistency, we follow the method of Wang et al. (2013). The dynamical mass within the disk radius is given by $M_{\text{dyn}} \approx 1.16 \times 10^5 v_{\text{cir}}^2 D M_{\odot}$ where D is the disk diameter in kpc and calculated as $1.5 \times$ the deconvolved Gaussian spatial FWHM. The resulting dynamical masses are given in Table 2. We note that there is considerable uncertainty on these values due to the unknown spatial and velocity structure of the gas, the marginal spatial resolution and limited sensitivity that means we may be missing more extended gas. Due to these uncertainties we do not place formal error bars on the dynamical masses, following Wang et al. (2013). Higher resolution data in the future are required to confirm the derived masses.

SDSS J1148+5251 has been extensively studied in [CII] (Maiolino et al. 2005; Walter et al. 2009; Maiolino et al. 2012; Ciccone et al. 2014). The highest resolution observations by Walter et al. (2009) revealed a very compact circumnuclear starburst with radius 0.75 kpc and $\text{FWHM}_{\text{[CII]}} = 287 \pm 28 \text{ km s}^{-1}$. For an assumed inclination of $i = 55^\circ$ this gives $M_{\text{dyn}} = 1.8 \times 10^{10} M_{\odot}$. For comparison Walter et al. (2004) determined a dynamical mass from CO emission in this quasar of $5.5 \times 10^{10} M_{\odot}$ within a larger radius of 2.5 kpc, the larger radius being the main difference between the results. Recent observations have shown more complex [CII] emission including evidence for gas extended over tens of kpc and at high velocities indicative of outflow (Maiolino et al. 2012; Ciccone et al. 2014). We adopt $M_{\text{dyn}} = 1.8 \times 10^{10} M_{\odot}$ for SDSS J1148+5251 noting that the true value could be several times larger. The most distant known quasar, ULAS J1120+0641 at $z = 7.08$, has been well detected in [CII], although not yet spatially resolved (Venemans et al. 2012). Based on the published $\text{FWHM}_{\text{[CII]}} = 235 \pm 35 \text{ km s}^{-1}$ and assuming a spatial FWHM of 3 kpc (similar to the other quasars resolved by ALMA) and $i = 55^\circ$ we determine $M_{\text{dyn}} = 2.4 \times 10^{10} M_{\odot}$.

In Figure 7 we plot black hole mass versus galaxy dynamical mass for the most distant known quasars. The

TABLE 2
MASS DETERMINATIONS FOR $z > 5.7$ QUASARS

Name	$z_{\text{[CII]}}$	$M_{\text{BH}} (M_{\odot})^a$	σ^b	$M_{\text{dyn}} (M_{\odot})$	Refs. ^c
CFHQS J0055+0146	6.0060 ± 0.0008	$(2.4^{+2.6}_{-1.4}) \times 10^8$	207 ± 45	4.2×10^{10}	1,2
CFHQS J0210-0456	6.4323 ± 0.0005	$(0.8^{+1.0}_{-0.6}) \times 10^8$	98 ± 20	1.3×10^{10}	1,2,3
CFHQS J2229+1457	6.1517 ± 0.0005	$(1.2^{+1.4}_{-0.8}) \times 10^8$	241 ± 51	4.4×10^{10}	1,2
SDSS J0129-0035	5.7787 ± 0.0001	$(1.7^{+3.1}_{-1.1}) \times 10^8$	112 ± 21	1.3×10^{10}	4
SDSS J1044-0125	5.7847 ± 0.0007	$(1.1^{+1.9}_{-0.7}) \times 10^{10}$	291 ± 76	— ^d	4
SDSS J1148+5251	6.4189 ± 0.0006	$(4.9^{+4.9}_{-2.5}) \times 10^9$	186 ± 38	1.8×10^{10}	5,6,7
SDSS J2054-0005	6.0391 ± 0.0001	$(0.9^{+1.6}_{-0.6}) \times 10^9$	364 ± 67	7.2×10^{10}	4
SDSS J2310+1855	6.0031 ± 0.0002	$(2.8^{+5.1}_{-1.8}) \times 10^9$	325 ± 61	9.6×10^{10}	4
ULAS J1120+0641	7.0842 ± 0.0004	$(2.4^{+2.4}_{-1.2}) \times 10^9$	144 ± 34	2.4×10^{10}	8,9
ULAS J1319+0950	6.1330 ± 0.0007	$(2.1^{+3.8}_{-1.4}) \times 10^9$	381 ± 91	12.5×10^{10}	4

NOTES.—

^a Derived from Mg II $\lambda 2799$ observations if possible, else from Eddington luminosity assumption. Uncertainties include observational errors plus systematics based on calibrations.

^b Derived from Gaussian FWHM fit to [C II] spectrum using method of Ho (2007b) including an inclination correction (see text for individual inclinations assumed). Uncertainties include observational errors plus systematics based on calibrations.

^c References: (1) This paper, (2) Willott et al. (2010a), (3) Willott et al. (2013), (4) Wang et al. (2013), (5) Maiolino et al. (2005), (6) Walter et al. (2009), (7) De Rosa et al. (2011), (8) Venemans et al. (2012), (9) De Rosa et al. (2014).

^d This quasar does not have a dynamical mass calculation in Wang et al. (2013) due to the difference in the [C II] and CO line profiles.

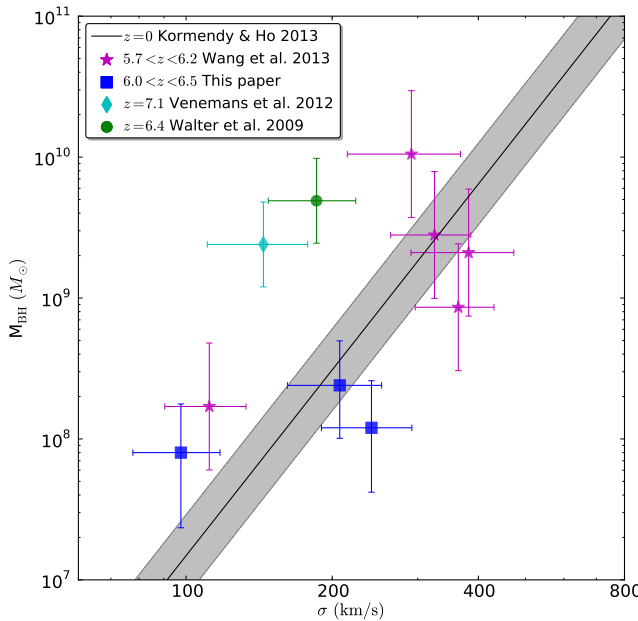


FIG. 6.— Black hole mass versus velocity dispersion calculated from the [C II] line using the method of Ho (2007b) for $z \approx 6$ quasars. Quasars from the CFHQS are shown as blue squares and the other symbols show quasars from the SDSS and ULAS surveys. The black line with gray shading is the local correlation $\pm 1\sigma$ scatter of black hole mass and bulge velocity dispersion (Kormendy & Ho 2013). The $z \approx 6$ quasars are distributed around the the local relationship, but with a much larger scatter and some quasars with significantly lower σ for their M_{BH} .

black line and gray shading represent the local correlation of M_{BH} with bulge mass M_{bulge} (Kormendy & Ho 2013). In the absence of gas accretion and mergers the present stellar bulge mass represents the sum of the gas and stellar mass at high-redshift, so it is a good comparison for the dynamical mass within the central few kpc. Kormendy & Ho (2013) note that their correlation (their equation 10) gives a black hole to bulge mass ratio of 0.5% at $M_{\text{bulge}} = 10^{11} M_{\odot}$ that is 2 to 4 times higher than previous estimates due to the omission of

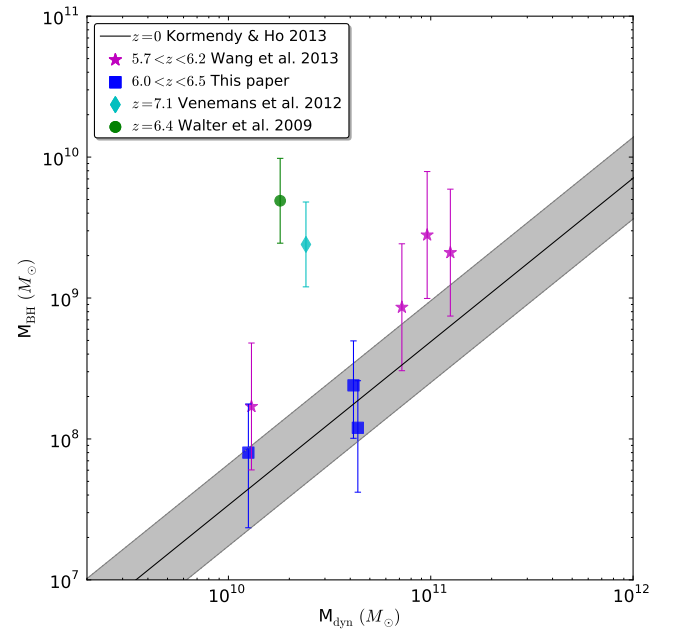


FIG. 7.— Black hole mass versus host galaxy dynamical mass for $z \approx 6$ quasars. Symbols as for Figure 6. The black line with gray shading is the local correlation $\pm 1\sigma$ scatter from the work of Kormendy & Ho (2013) equating M_{dyn} to M_{bulge} . The CFHQS quasars lie on the local relationship and do not show the large offset displayed by the most massive black holes. Uncertainties in M_{dyn} have not been calculated due to the reasons given in the text.

pseudobulges, galaxies with uncertain M_{BH} and ongoing mergers.

The position of the high- z data with respect to low redshift is fairly similar to Figure 6, not surprising because v_{cir} derived from the [C II] velocity FWHM is a major factor in both σ and M_{dyn} . The points are shifted somewhat further from the local bulge mass than for the local velocity dispersion. This shift is due to the smaller size of galaxies at high-redshift, as the size is the only term in the derivation of dynamical mass not in σ . We note the much greater dynamic range in black hole mass

(2 dex) than in dynamical mass (1 dex) in our sample. This is likely due more to our selection over a wide range of quasar luminosity than to a non-linear relationship between these quantities at $z = 6$.

All three of the CFHQS quasars lie within the local 1σ scatter and the one $M_{\text{BH}} \sim 10^8 M_{\odot}$ quasar in Wang et al. (2013) is only a factor of 4 greater than the local relationship. In contrast the $M_{\text{BH}} > 10^9 M_{\odot}$ quasars tend to show a larger scatter and larger offset above the local relationship as previously found (Walter et al. 2004; Wang et al. 2010; Venemans et al. 2012; Wang et al. 2013). We caution that there are considerable uncertainties in some of these measurements as already discussed, but in dynamical mass the results look more like we would expect based on the quasar selection bias effect.

5. CONCLUSIONS

During ALMA Early Science cycles 0 and 1 we have observed a complete sample of four $z > 6$ moderate luminosity CFHQS quasars with black hole masses $\sim 10^8 M_{\odot}$. Three of the four are detected in both far-IR continuum and the [C II] emission line. The far-IR luminosity is found to be substantially lower than that of similar luminosity quasars at $1 < z < 3$. Assuming that far-IR luminosity traces star formation equally effectively at these redshifts this implies that at $z \approx 6$ quasars are growing their black holes more rapidly than their stellar mass compared to at the peak of the *quasar epoch* ($1 < z < 3$).

The ratios of [CII] to far-IR luminosities for the CFHQS quasars lie in the range 0.001 to 0.01, similar to that of low-redshift galaxies at the same far-IR luminosity. This suggests a similar mode of star-formation spread throughout the host galaxy (rather than in dense circumnuclear starburst regions that have lower values for this ratio in local ULIRGs). Combining with previous $z > 5.7$ quasar data at higher L_{FIR} we find that the far-IR luminosity dependence of the [C II]/FIR ratio has a shallow negative slope, possibly due in part to an increase in L_{FIR} due to quasar-heated dust in some optically-luminous high- z quasars.

The three CFHQS quasars well-detected in the [C II] emission line allow this atomic gas to be used as a tracer of the host galaxy dynamics. Combining with published data on higher black hole mass quasars we have investigated the $M_{\text{BH}} - \sigma$ and $M_{\text{BH}} - M_{\text{dyn}}$ relations at $z \approx 6$. We show that the $z = 6$ quasars display a $M_{\text{BH}} - \sigma$ rela-

tion with similar slope and normalization to locally, but with much greater scatter. Similar results are obtained for the $M_{\text{BH}} - M_{\text{dyn}}$ relation with a somewhat higher normalization at $z = 6$ and a higher scatter at high M_{BH} . As discussed in

Combining our results on the relatively low L_{FIR} for $M_{\text{BH}} \sim 10^8 M_{\odot}$ $z \approx 6$ quasars with their location on the $M_{\text{BH}} - \sigma$ relation leads to something of a paradox. The fact these quasars lie on the local $M_{\text{BH}} - \sigma$ relation suggests that their host galaxies have undergone considerable evolution to acquire such a high dynamical mass. So why is it that this mass accumulation is not leading to a high star formation rate? As discussed in Wi13, simulations such as those of Khandai et al. (2012) and Lapi et al. (2014) predict that such low ratios of SFR to black hole accretion occur after episodes of strong feedback that inhibits star formation throughout quasar host galaxies. Another possibility mentioned in Section 4.1 is that L_{FIR} fails to trace star formation so effectively in these high-redshift galaxies, due to lower dust content (e.g. Ouchi et al. 2013). Note that using $L_{\text{[CII]}}$ as a star formation rate tracer instead of L_{FIR} , would give higher SFR by a factor of three for one of the CFHQS quasars.

Higher resolution follow-up [C II] observations of these quasars are critical to measure more accurately the distribution and kinematics of the gas used as a dynamical tracer in order to reliably determine the location and scatter of the correlations between black holes and their host galaxies at high-redshift.

Thanks to staff at the North America ALMA Regional Center for processing the ALMA data. Thanks to Melanie Veale for useful discussion and providing her models in electronic form. This paper makes use of the following ALMA data: ADS/JAO.ALMA#2012.1.00676.S. ALMA is a partnership of ESO (representing its member states), NSF (USA) and NINS (Japan), together with NRC (Canada) and NSC and ASIAA (Taiwan), in cooperation with the Republic of Chile. The Joint ALMA Observatory is operated by ESO, AUI/NRAO and NAOJ. The National Radio Astronomy Observatory is a facility of the National Science Foundation operated under cooperative agreement by Associated Universities, Inc.

Facility: ALMA.

REFERENCES

Bonfield, D. G., Jarvis, M. J., Hardcastle, M. J., et al. 2011, MNRAS, 416, 13

Bouwens, R. J., Illingworth, G. D., Oesch, P. A., et al. 2014, ArXiv e-prints, arXiv:1403.4295

Carilli, C. L., & Walter, F. 2013, ARA&A, 51, 105

Carilli, C. L., Wang, R., Fan, X., et al. 2010, ApJ, 714, 834

Cassata, P., Giavalisco, M., Guo, Y., et al. 2011, ApJ, 743, 96

Chary, R., & Elbaz, D. 2001, ApJ, 556, 562

Cicone, C., Maiolino, R., Gallerani, S., et al. 2014, ArXiv e-prints, arXiv:1409.4418

Cisternas, M., Jahnke, K., Bongiorno, A., et al. 2011, ApJ, 741, L11

De Looze, I., Cormier, D., Lebouteiller, V., et al. 2014, A&A, 568, A62

De Rosa, G., Decarli, R., Walter, F., et al. 2011, ApJ, 739, 56

De Rosa, G., Venemans, B. P., Decarli, R., et al. 2014, ApJ, 790, 145

Farrah, D., Lebouteiller, V., Spoon, H. W. W., et al. 2013, ApJ, 776, 38

Fine, S., Croom, S. M., Miller, L., et al. 2006, MNRAS, 373, 613

Fisher, D. B., Bolatto, A. D., Herrera-Camus, R., et al. 2014, Nature, 505, 186

Freudling, W., Corbin, M. R., & Korista, K. T. 2003, ApJ, 587, L67

Graciá-Carpio, J., Sturm, E., Hailey-Dunsheath, S., et al. 2011, ApJ, 728, L7

Hickox, R. C., Mullaney, J. R., Alexander, D. M., et al. 2014, ApJ, 782, 9

Ho, L. C. 2007a, ApJ, 668, 94

—. 2007b, ApJ, 669, 821

Jiang, L., Fan, X., Vestergaard, M., et al. 2007, AJ, 134, 1150

Khandai, N., Feng, Y., DeGraf, C., Di Matteo, T., & Croft, R. A. C. 2012, MNRAS, 423, 2397

Kormendy, J., & Ho, L. C. 2013, ARA&A, 51, 511

Kurk, J. D., Walter, F., Fan, X., et al. 2007, ApJ, 669, 32

Lapi, A., Raimundo, S., Aversa, R., et al. 2014, ApJ, 782, 69

Lauer, T. R., Tremaine, S., Richstone, D., & Faber, S. M. 2007, ApJ, 670, 249

Magdis, G. E., Rigopoulou, D., Hopwood, R., et al. 2014, *ApJ*, 796, 63

Maiolino, R., Cox, P., Caselli, P., et al. 2005, *A&A*, 440, L51

Maiolino, R., Gallerani, S., Neri, R., et al. 2012, *MNRAS*, 425, L66

McGreer, I. D., Jiang, L., Fan, X., et al. 2013, *ApJ*, 768, 105

Mechtley, M., Windhorst, R. A., Ryan, R. E., et al. 2012, *ApJ*, 756, L38

Merloni, A., Bongiorno, A., Bolzonella, M., et al. 2010, *ApJ*, 708, 137

Omont, A., Willott, C. J., Beelen, A., et al. 2013, *A&A*, 552, A43

Ota, K., Walter, F., Ohta, K., et al. 2014, *ApJ*, 792, 34

Ouchi, M., Ellis, R., Ono, Y., et al. 2013, *ApJ*, 778, 102

Park, D., Woo, J.-H., Bennert, V. N., et al. 2014, *ArXiv e-prints*, [arXiv:1411.6334](https://arxiv.org/abs/1411.6334)

Peng, C. Y. 2007, *ApJ*, 671, 1098

Planck Collaboration. 2014, *A&A*, 571, A16

Rawle, T. D., Egami, E., Bussmann, R. S., et al. 2014, *ApJ*, 783, 59

Richards, G. T., Vanden Berk, D. E., Reichard, T. A., et al. 2002, *AJ*, 124, 1

Riechers, D. A., Bradford, C. M., Clements, D. L., et al. 2013, *Nature*, 496, 329

Rosario, D. J., Santini, P., Lutz, D., et al. 2012, *A&A*, 545, A45

Rosario, D. J., Trakhtenbrot, B., Lutz, D., et al. 2013, *A&A*, 560, A72

Sargsyan, L., Samsonyan, A., Lebouteiller, V., et al. 2014, *ApJ*, 790, 15

Sargsyan, L., Lebouteiller, V., Weedman, D., et al. 2012, *ApJ*, 755, 171

Schulze, A., & Wisotzki, L. 2014, *MNRAS*, 438, 3422

Serjeant, S., Bertoldi, F., Blain, A. W., et al. 2010, *A&A*, 518, L7

Shen, Y., Greene, J. E., Strauss, M. A., Richards, G. T., & Schneider, D. P. 2008, *ApJ*, 680, 169

Shen, Y., & Kelly, B. C. 2012, *ApJ*, 746, 169

Sijacki, D., Vogelsberger, M., Genel, S., et al. 2014, *ArXiv e-prints*, [arXiv:1408.6842](https://arxiv.org/abs/1408.6842)

Stacey, G. J., Hailey-Dunsheath, S., Ferkinhoff, C., et al. 2010, *ApJ*, 724, 957

Tan, Q., Daddi, E., Sargent, M., et al. 2013, *ApJ*, 776, L24

Targett, T. A., Dunlop, J. S., & McLure, R. J. 2012, *MNRAS*, 420, 3621

Trakhtenbrot, B., Netzer, H., Lira, P., & Shemmer, O. 2011, *ApJ*, 730, 7

Veale, M., White, M., & Conroy, C. 2014, *MNRAS*, 445, 1144

Venemans, B. P., McMahon, R. G., Walter, F., et al. 2012, *ApJ*, 751, L25

Walter, F., Carilli, C., Bertoldi, F., et al. 2004, *ApJ*, 615, L17

Walter, F., Riechers, D., Cox, P., et al. 2009, *Nature*, 457, 699

Wandel, A., Peterson, B. M., & Malkan, M. A. 1999, *ApJ*, 526, 579

Wang, R., Carilli, C. L., Neri, R., et al. 2010, *ApJ*, 714, 699

Wang, R., Wagg, J., Carilli, C. L., et al. 2011, *AJ*, 142, 101

—. 2013, *ApJ*, 773, 44

Willott, C. J., Omont, A., & Bergeron, J. 2013, *ApJ*, 770, 13

Willott, C. J., Percival, W. J., McLure, R. J., et al. 2005, *ApJ*, 626, 657

Willott, C. J., Albert, L., Arzoumanian, D., et al. 2010a, *AJ*, 140, 546

Willott, C. J., Delorme, P., Reylé, C., et al. 2010b, *AJ*, 139, 906